

# Combining dynamin 2 myopathy and neuropathy mutations rescues both phenotypes

Received: 7 June 2024

Accepted: 2 May 2025

Published online: 20 May 2025

Marie Goret<sup>1</sup>, Evelina Edelweiss<sup>1</sup>, Jérémy Jehl<sup>1</sup>, David Reiss<sup>1</sup>,  
Patricio Aguirre-Pineda<sup>2</sup>, Sylvie Friant<sup>2</sup> & Jocelyn Laporte<sup>1</sup>✉

Mutations within a single gene can lead to diverse human genetic diseases affecting highly specialized tissues. Notably, dominant mutations in the *DNM2* gene, encoding the mechanoenzyme dynamin, lead to distinct neuromuscular disorders: centronuclear myopathy (CNM) and Charcot-Marie-Tooth neuropathy (CMT). CNM is characterized by myofiber structural anomalies while CMT presents peripheral nerve defects, both culminating in muscle weakness and atrophy. Despite their shared genetic origin, the mechanisms driving these diseases remain elusive, and no cure is available. Here, we present in vitro assays underlining opposing effects of *DNM2* mutations, gain-of-function in CNM and loss-of-function in CMT. In vivo, we explored the potential compensatory effects of CNM and CMT mutations by breeding *Dnm2*<sup>S619L/+</sup> CNM with *Dnm2*<sup>K562E/+</sup> CMT mouse models. *Dnm2*<sup>S619L/K562E</sup> offspring exhibit strongly improved motor coordination and muscle strength and mass, compared to single-mutant littermates. *Dnm2*<sup>S619L/K562E</sup> mice present normalized muscle structure and nerve fiber organization. This study reveals that two distinct disease-causing mutations within the *DNM2* gene compensate each other in vivo, leading to corrections of most individual phenotypes. The inverse modulation of *DNM2* activity emerges as a promising therapeutic strategy to address CNM and CMT diseases.

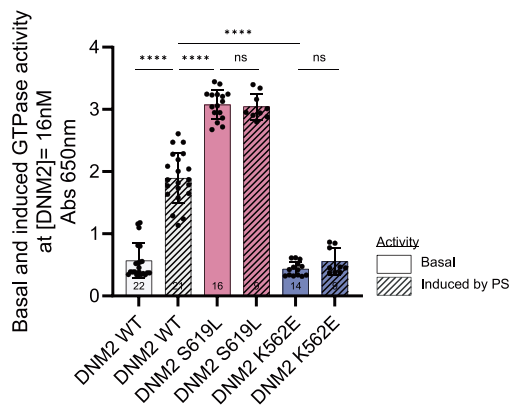
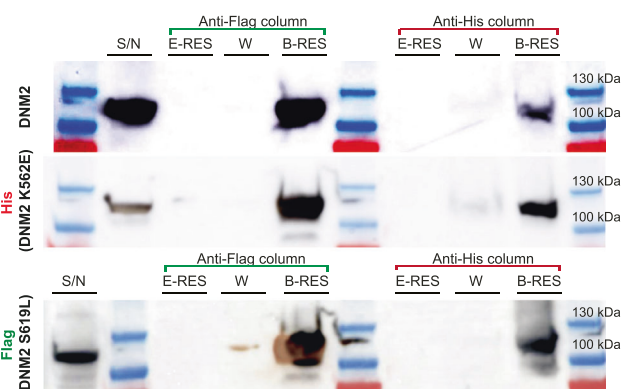
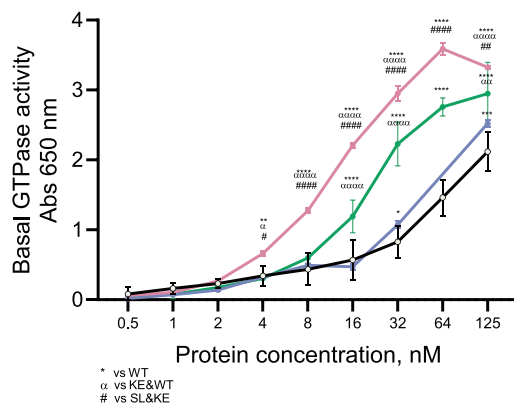
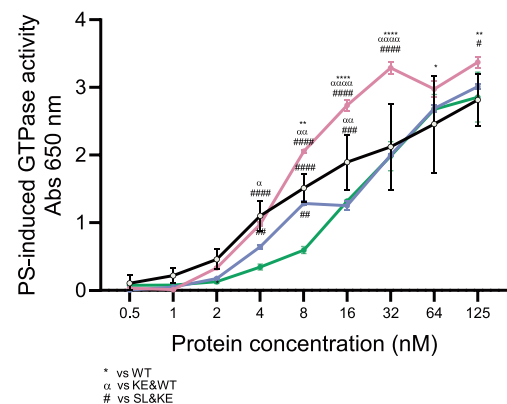
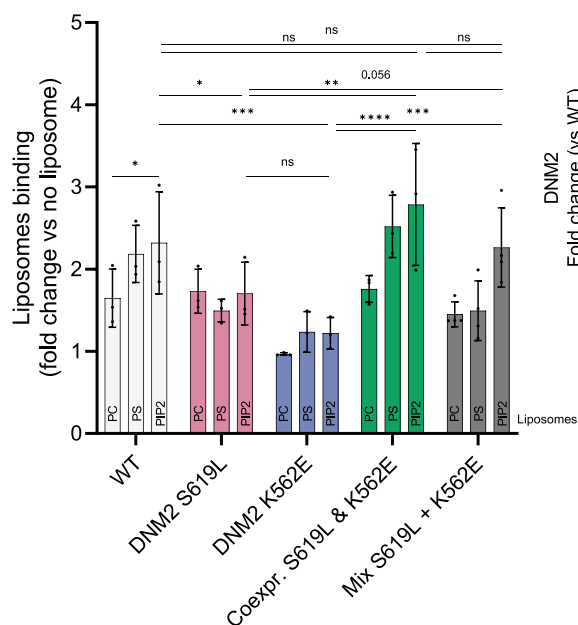
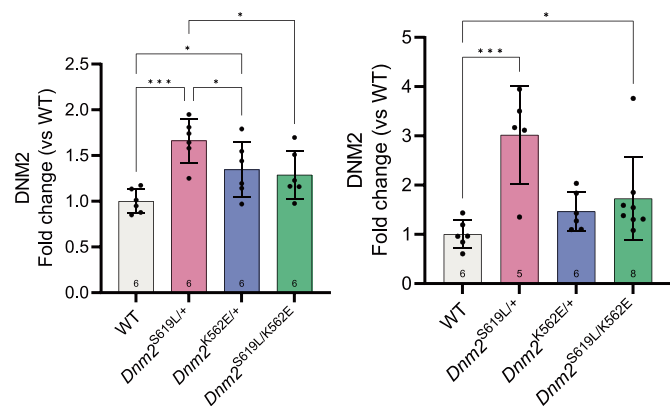
As a member of the dynamin family of large GTPases<sup>1</sup>, Dynamin 2 (*DNM2*) exhibits ubiquitous expression and is a key regulator of membrane fission and trafficking<sup>2,3</sup>. The binding of dynamin to lipid membrane via its Pleckstrin Homology (PH) domain triggers its oligomerization via the stalk domain and enhances its GTPase activity, ultimately correlating with membrane fission<sup>4</sup>. Dominant mutations in the *DNM2* gene lead to distinct neuromuscular disorders: centronuclear myopathy (CNM) and Charcot-Marie-Tooth neuropathy (CMT)<sup>5–7</sup>. Most *DNM2*-CNM and CMT mutations are localized in the PH domain<sup>4,8,9</sup>. CNM mutations are predicted to disturb the interaction between the PH and stalk domains, promoting an active

conformation<sup>10</sup>, while CMT mutations are predicted to impair lipid binding and GTPase activity<sup>11–13</sup>.

The S619L heterozygous mutation is the most common in patients with dominant CNM and a severe neonatal onset (MIM#160150)<sup>8,9</sup>. The *Dnm2*<sup>S619L/+</sup> knock-in mouse recapitulates the muscle weakness and atrophy associated with specific histopathological hallmarks as mispositioning of nuclei and other organelles in myofibers<sup>14</sup>. The K562E heterozygous missense is the most prevalent mutation causing a dominant intermediate form of CMT (DI-CMTB; MIM#606482)<sup>6</sup>. Patients experience progressive muscle weakness and atrophy, particularly in the distal extremities, sensory loss, and

<sup>1</sup>Institute of Genetics and Molecular and Cellular Biology (IGBMC), INSERM U1258, CNRS UMR7104, University of Strasbourg, 1 rue Laurent Fries, 67404 Illkirch, France. <sup>2</sup>Medical Genetics Laboratory, INSERM UMRS 1112, University of Strasbourg, CRBS, 1 rue Eugène Boeckel, 67000 Strasbourg, France.

✉ e-mail: [jocelyn@igbmc.fr](mailto:jocelyn@igbmc.fr)

**A Basal and PS-induced DNM2 mutants GTPase activity****B Western blot - pull down experiment 1****C Basal DNM2 mutants GTPase activity in heterozygous mixes****D PS-induced DNM2 mutants GTPase activity in heterozygous mixes****E Liposomes binding assay****F Western blot DNM2 in TA muscle, and G in sciatic nerve**

foot deformities. Main histological defects include axonal degeneration, loss of large myelinated fibers and/or myelin defects in peripheral nerves<sup>15</sup>. In accordance, the *Dnm2*<sup>K562E/+</sup> mouse displays motor deficit and muscle atrophy together with mild peripheral nerve defects<sup>16</sup>.

We hypothesize a gain-of-function scenario for CNM and a loss-of-function mechanism for CMT in a physiological context. If true, we predict the simultaneous presence of both CNM and CMT mutations would lead to a compensatory effect, potentially mitigating individual disease manifestations, and providing a basis for potential therapeutic strategies.

**Fig. 1 | Opposite functional impact of *DNM2*-CNM and CMT mutations.** **A** Basal and phosphatidylserine (PS) induced GTPase activity of rDNM2 mutants at 16 nM ( $9 \leq n \leq 22$ ,  $^{***}P < 0.0001$ ). **B** Representative western blots of infected Sf21 cells supernatant (S/N), empty-resin (E-RES), wash (W) and bound-resin (B-RES) from pull-down experiment 1, probed with anti-DNM2, anti-His and anti-Flag antibodies. Experiment performed in technical triplicates. **C, D** (**C**) Basal ( $n$  WT = 20,  $n$  SL&WT = 3,  $n$  KE&WT = 3,  $n$  SL&KE = 6, from left to right  $^{**}P = 0.0071$ ,  $^{*}P = 0.0322$ ,  $^{*}P = 0.0237$ ,  $^{*}P = 0.0366$ ,  $^{*}P = 0.0056$ ,  $^{*}P = 0.0017$ ,  $^{***}P = 0.0007$ ,  $^{####}P < 0.0001$ ); and (**D**) PS-induced GTPase activity of heterozygous rDNM2 mutant mixes at various concentrations ( $n$  WT = 15,  $n$  SL&WT = 3,  $n$  KE&WT = 3,  $n$  SL&KE = 6, from left to right  $^{*}P = 0.0313$ ,  $^{*}P = 0.0257$ ,  $^{*}P = 0.0070$ ,  $^{*}P = 0.0083$ ,  $^{*}P = 0.0047$ ,  $^{*}P = 0.0035$ ,  $^{*}P = 0.0018$ ,  $^{*}P = 0.0002$ ,  $^{*}P = 0.0127$ ,  $^{*}P = 0.0067$ ,  $^{*}P = 0.0281$ ,  $^{####}P < 0.0001$ ). **E** Binding of the indicated rDNM2 proteins (WT, S619L, K562E, co-expressed S619L + K562E (Coexp), or equimolar mix (Mix)) to liposomes

with 100% PC, 3% PS or 3% of PIP2 in a PC background. Binding was assessed by liposome co-sedimentation and normalized to the no-liposome condition ( $3 \leq n \leq 4$ , from left to right  $^{*}P = 0.0332$ ,  $^{*}P = 0.0498$ ,  $^{*}P = 0.0009$ ,  $^{*}P = 0.0011$ ,  $^{***}P < 0.0001$ ,  $^{***}P = 0.0008$ ). **F, G** Western blots quantifications of DNM2 protein level in (**F**) TA ( $n = 6$ , from left to right  $^{***}P = 0.0001$ ,  $^{*}P = 0.0221$ ,  $^{*}P = 0.0361$ ,  $^{*}P = 0.0149$ ), and (**G**) sciatic nerve ( $5 \leq n \leq 8$ ,  $^{***}P = 0.0007$ ,  $^{*}P = 0.0256$ ) of 8 weeks-old mice. **A, E** Each dot represents an experiment. **C, D** Each  $n$  represents an experiment, and the graph shows mean  $\pm$  SD. **F, G** Each dot represents a mouse. Values are represented as mean  $\pm$  SD. In (**C, D**) significant differences vs WT, KE&WT, or SL&KE groups were indicated with \*,  $\alpha$ , and # respectively. **A–F** Two-sided ANOVA test. **G** Two-sided Kruskal–Wallis test. In (**E**) statistics are shown for different liposome compositions in WT and for PIP2 liposomes across proteins. Source data are provided as a Source Data file.

## Results

### Opposite functional impact of *DNM2*-CNM and CMT mutations

Both DNM2 S619L-CNM and K562E-CMT mutations localize to the PH domain, albeit on distant sites (Supplementary Fig. 1A). The S619L mutation likely disrupts PH-stalk interaction, leading to an open active conformation, while K562E likely affects lipid binding. To investigate the functional impact of *DNM2*-CNM and CMT mutations, GTPase activity assays were performed using recombinant DNM2 (rDNM2) with and without phosphatidylserine (PS) lipid supplementation. While rDNM2-WT (wild-type) showed a 3.3-fold increase in activity with lipid, neither rDNM2-SL nor rDNM2-KE responded to lipid, confirming their lipid-uncoupled nature<sup>12</sup> (Fig. 1A). The rDNM2-SL exhibited a 1.6-fold higher activity than lipid-induced rDNM2-WT, whereas rDNM2-KE displayed an averaged 3.9-fold reduced activity, confirming both gain and loss-of-function respectively.

rDNM2 mutants interaction was studied by pull-down assays from Flag-tagged-rDNM2-SL and His-tagged-rDNM2-KE mutants co-infected in insect cells (Supplementary Fig. 1B). Both rDNM2-SL and rDNM2-KE mutants were recovered from either anti-Flag or anti-His columns, supporting their direct interaction (Fig. 1B, Supplementary Fig. 1C, experiment 1). In addition, eluate from the anti-Flag column was reloaded onto an anti-His column and both proteins were again recovered (Supplementary Fig. 1C, D, experiment 2).

To mimic a disease-relevant environment, the GTPase activity was assessed under ‘heterozygous’ conditions by combining proteins in pairs. Under basal conditions, the SL&WT mix consistently exhibited elevated GTPase activity compared to other conditions (Fig. 1C). The activity of the SL&KE was intermediate between SL&WT and KE&WT. Upon lipid supplementation, the SL&WT mix sustained elevated activity. In contrast, the SL&KE demonstrated either comparable or reduced activity relative to WT (Fig. 1D).

Previous studies reported that *DNM2* mutants have an impact on lipid binding<sup>12</sup>. Using liposome co-sedimentation experiments with different composition, PC 100% or bearing 3% of PI(4,5)P2 (PIP2) or 3% of PS in a PC background and recombinant DNM2 proteins, we confirmed rDNM2-WT binds liposomes and this binding is enhanced by the addition of PIP2 (Fig. 1E, Supplementary Fig. 2). Noteworthy, it binds equally to PS and PIP2. The data show that the rDNM2-KE is defective in PIP2 binding, consistent with the localization of this mutation in the lipid-binding loop. To determine the effect of combining the rDNM2-SL CNM mutant with the rDNM2-KE CMT mutant on the membrane binding, we either co-expressed both mutants in insect cells and purified the proteins as a complex (Coexpr), or we analyzed an equimolar mixture of purified rDNM2-SL and rDNM2-KE (Mix). We found that the SL&KE hetero-oligomers normalized the binding to PIP2 liposomes to WT level compared to rDNM2-KE alone, similarly in the Coexpr and Mix conditions.

Overall, we confirmed gain and loss-of-function impact of *DNM2*-CNM and CMT mutations, respectively, and revealed the combination

of both mutations rescued the abnormally high GTPase activity of the S619L mutation and the defective lipid binding of the K562E mutation; restoring their respective major biochemical abnormalities.

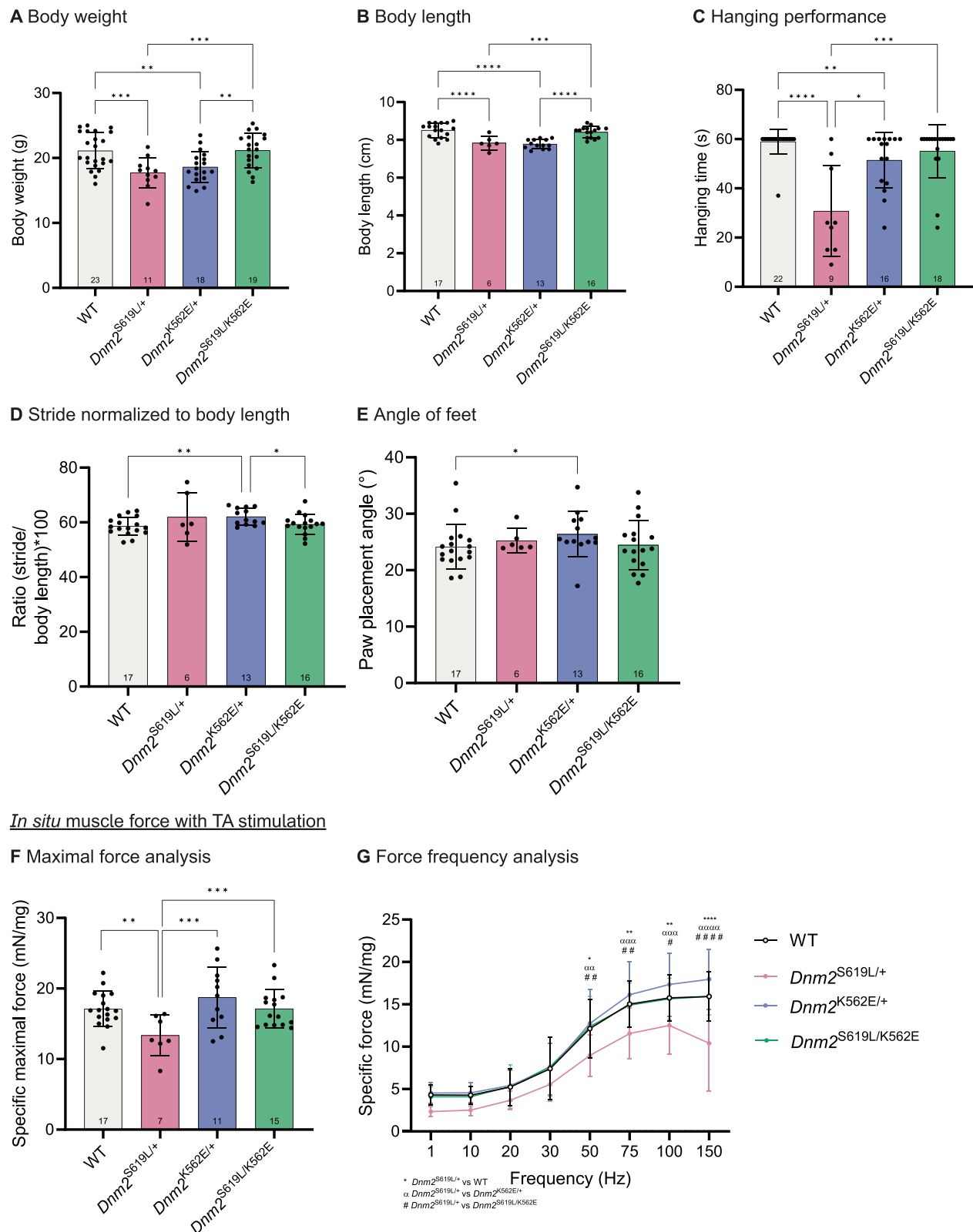
### CNM and CMT mutations antagonize each other to restore whole-body motor performance

To explore the potential compensatory effects of both *DNM2*-CNM and CMT mutations in vivo, we crossed the *Dnm2*<sup>S619L/+</sup> CNM and *Dnm2*<sup>K562E/+</sup> CMT mouse models<sup>14,16</sup> and compared their behavioral and locomotor activities with *Dnm2*<sup>S619L/K562E</sup> littermates at 8 weeks of age. Of note, *Dnm2*<sup>S619L/S619L</sup> mice exhibit perinatal lethality<sup>14</sup> while *Dnm2*<sup>K562E/K562E</sup> died during early embryogenesis before E18.5 (Supplementary Fig. 3). Noteworthy, Ferguson et al.<sup>17</sup> and Cowling et al.<sup>18</sup> found the constitutive *Dnm2* knockout is embryonic lethal, suggesting the critical role of a DNM2 activity for mammalian development. However, our study demonstrates the viability of *Dnm2*<sup>S619L/K562E</sup> mice for at least 52 weeks in the absence of any WT protein (Supplementary Fig. 4A–C). Both mutations were expressed at equivalent RNA level in *Dnm2*<sup>S619L/K562E</sup> mice (Supplementary Fig. 4D–F), while DNM2 protein level was overexpressed in Tibialis anterior (TA) muscle and sciatic nerves in *Dnm2*<sup>S619L/+</sup> mice and only in TA in *Dnm2*<sup>K562E/+</sup> mice compared to WT, and normalized in TA in *Dnm2*<sup>S619L/K562E</sup> mice compared to *Dnm2*<sup>S619L/+</sup> mice (Fig. 1F, G, Supplementary Fig. 4G, H).

*Dnm2*<sup>S619L/+</sup> and *Dnm2*<sup>K562E/+</sup> mice presented a lower body weight and length and decreased motor performance than WT (Fig. 2A–C, Supplementary Fig. 5A–C). All these defects were restored in *Dnm2*<sup>S619L/K562E</sup> mice. As patients, mice carrying the *Dnm2*-CMT mutation presented coordination defects, as evidenced by increased stride length (106%) and feet angle (+2.2°) compared to WT (Fig. 2D, E). The presence of the CNM mutation in *Dnm2*<sup>S619L/K562E</sup> mice rescued the abnormal stride and improved the feet angle. *Dnm2*<sup>S619L/+</sup> mice demonstrated a reduced maximal ( $\Delta = -22\%$ ) and submaximal in situ TA muscle force, while *Dnm2*<sup>K562E/+</sup> mice showed no significant changes compared to WT (Fig. 2F, G, Supplementary Fig. 5D, E). The presence of the CMT mutation in *Dnm2*<sup>S619L/K562E</sup> mice counteracted the muscle weakness observed in CNM mice. Overall, the motor function defect observed in *Dnm2*<sup>S619L/+</sup> mice is caused by coordination defects, while it is mainly due to muscle weakness in *Dnm2*<sup>S619L/+</sup> mice. Both phenotypes were normalized by the combined presence of the CNM and CMT mutations.

### Combining CNM and CMT mutations restores muscle organization

To elucidate the mechanisms underlying alterations in motor performance and muscle force, we explored muscle mass and myofiber structure. TA mass was reduced in *Dnm2*<sup>S619L/+</sup> (by 26%) and *Dnm2*<sup>K562E/+</sup> (16%) mice compared to WT, and such muscle atrophy correlated with myofiber hypotrophy but not with altered myofiber number (Fig. 3A–C, Supplementary Fig. 6A). These defects were partially rescued or normalized, respectively, in *Dnm2*<sup>S619L/K562E</sup> mice. Further



exploration into the molecular pathways underlying myofiber hypotrophy revealed no major alteration in mTOR activity, Ubiquitin-Proteasome System or autophagy between the mouse genotypes (Supplementary Fig. 6B–E)<sup>19</sup>.

Fiber morphology and organelle positioning were assessed in TA with hematoxylin-eosin (HE) and succinate dehydrogenase (SDH) staining. The histopathological hallmarks of CNM (rounder myofibers,

mislocalized nuclei and abnormal accumulation of oxidative staining depicting mitochondria organization) was evidenced in the *Dnm2*<sup>S619L/+</sup> mice but not found in the *Dnm2*<sup>K562E/+</sup> mice (Fig. 3D, Supplementary Fig. 7A–D). These CNM hallmarks were greatly ameliorated in the *Dnm2*<sup>S619L/K562E</sup> mice. Albeit no mitochondrial mispositioning was found in *Dnm2*<sup>K562E/+</sup> mice, a decrease of cytochrome C protein expression was found in their TA muscles compared to WT, suggesting



**Fig. 2 | CNM and CMT mutations antagonize each other to restore whole-body motor performance.** **A** Body weight of WT, *Dnm2*<sup>S619L/+</sup>, *Dnm2*<sup>K562E/+</sup> and *Dnm2*<sup>S619L/K562E</sup> mice at 8 weeks (11 ≤ n ≤ 23, from left to right <sup>\*\*\*</sup>P = 0.0007, <sup>\*\*\*</sup>P = 0.0028, <sup>\*\*\*</sup>P = 0.0008, <sup>\*\*\*</sup>P = 0.0034). **B** Body length measured with gait analysis. Measurement from the nose of the animal to the start of the tail (6 ≤ n ≤ 17, <sup>\*\*\*</sup>P = 0.0004, <sup>\*\*\*</sup>P < 0.0001). **C** Hanging test performance. Maximum hanging time = 60 s (9 ≤ n ≤ 22, <sup>\*\*\*</sup>P < 0.0001, <sup>\*\*\*</sup>P = 0.0044, <sup>\*\*\*</sup>P = 0.0166, <sup>\*\*\*</sup>P = 0.0002). **D** Stride (= length of a step) during treadmill walking normalized to body length (6 ≤ n ≤ 17, <sup>\*\*\*</sup>P = 0.0057, <sup>\*\*\*</sup>P = 0.0329). **E** Angle of feet between paw and body line during treadmill walking (6 ≤ n ≤ 17, <sup>\*\*\*</sup>P = 0.0297). **F** Maximal force developed by TA muscle when stimulating the TA at 150 Hz, normalized to TA mass (7 ≤ n ≤ 17, from left to

right <sup>\*\*\*</sup>P = 0.0031, <sup>\*\*\*</sup>P = 0.0005, <sup>\*\*\*</sup>P = 0.0035). **G** Force developed by TA muscle when stimulating the TA at different incremental frequencies (1–150 Hz), normalized to TA mass (n WT = 17, *Dnm2*<sup>S619L/+</sup> = 7, *Dnm2*<sup>K562E/+</sup> = 11, *Dnm2*<sup>S619L/K562E</sup> = 15, from left to right <sup>\*\*\*</sup>P = 0.0102, <sup>\*\*\*</sup>P = 0.0046, <sup>\*\*\*</sup>P = 0.0070, <sup>\*\*\*</sup>P = 0.0047, <sup>\*\*\*</sup>P = 0.0005, <sup>\*\*\*</sup>P = 0.0074, <sup>\*\*\*</sup>P = 0.0083, <sup>\*\*\*</sup>P = 0.0003, <sup>\*\*\*</sup>P = 0.0118, <sup>\*\*\*</sup>P < 0.0001). **G** Each n represents a mouse, and the graph shows mean ± SD. **A–F** Each dot represents a mouse. Values are represented as mean ± SD. In **(G)** significant differences between *Dnm2*<sup>S619L/+</sup> and WT, *Dnm2*<sup>K562E/+</sup> or *Dnm2*<sup>S619L/K562E</sup> groups were indicated with \*, α, and # respectively. **A–G** Two-sided ANOVA test. **C, E** Two-sided Kruskal-Wallis test. Source data are provided as a Source Data file.

mitochondrial dysfunction (Supplementary Fig. 7E). This defect was normalized with the concomitant presence of the S619L mutation. Ultrastructural analyses confirmed organelle misposition in *Dnm2*<sup>S619L/+</sup> fibers and identified fibrosis, which was further examined by immunofluorescence (Fig. 3E, Supplementary Fig. 7F). Collagen thickness was found to be increased in both single mutants but normalized in double mutants. Additionally, Z-line misalignment was observed in *Dnm2*<sup>S619L/+</sup> fibers (Fig. 3E, Supplementary Fig. 8A), while mitochondria were smaller in *Dnm2*<sup>K562E/+</sup> and rounder in both *Dnm2*<sup>S619L/+</sup> and *Dnm2*<sup>K562E/+</sup> fibers (Supplementary Fig. 8B, C). Notably, all these defects were either improved or fully rescued in *Dnm2*<sup>S619L/K562E</sup> muscles.

Immunofluorescence analyses of *Dnm2*<sup>S619L/+</sup> and *Dnm2*<sup>K562E/+</sup> muscles revealed abnormal localization of β1-integrin, an adhesion molecule trafficking in a dynamin-dependent pathway<sup>20</sup>, and abnormal localization and increased levels of desmin, a key marker of cytoskeletal organization (Fig. 3F, Supplementary Fig. 8D–F). These markers were normalized in *Dnm2*<sup>S619L/K562E</sup> fibers.

Overall, the presence of both CNM and CMT mutations in *Dnm2*<sup>S619L/K562E</sup> mice prevented muscle atrophy and maintained the structural integrity of myofibers, while also mitigating the typical histopathological hallmarks of CNM specific to the *Dnm2*<sup>S619L/+</sup> mice.

### Combining CNM and CMT mutations improves peripheral nerve defects

Considering the neuropathic nature of the CMT condition and the motor coordination defects of the *Dnm2*<sup>K562E/+</sup> mice, our investigation extended to the peripheral nervous system. No discernible impairments in thermal or mechanical sensitivity were observed across all mouse genotypes (Supplementary Fig. 9A–C).

In most genotypes, TA muscle force measurements were similar whether stimulated directly (Fig. 2G) or via the sciatic nerve (Supplementary Fig. 9D). However, *Dnm2*<sup>S619L/+</sup> mice showed lower muscle force following nerve stimulation compared to muscle stimulation, suggesting potential conduction impairments (Supplementary Fig. 9E). This observation may indicate muscle denervation, supported by increased expression of acetylcholine receptor subunits α (*Chrna1*) and γ (*Chrng*), with stable levels of ε (*Chrne*)<sup>21</sup> (Fig. 4A–C). In contrast, the increased expression of *Chrna1* and *Chrng* in *Dnm2*<sup>K562E/+</sup> mice, along with elevated *Chrne* levels, likely reflects enhanced sub-synaptic nuclei activity rather than denervation. Despite these indications of potential conduction impairments and muscle denervation in *Dnm2*<sup>S619L/+</sup> mice, aspecific esterase staining of TA muscle sections did not reveal significant morphological anomalies at the neuromuscular junctions nor the presence of denervated fibers (Supplementary Fig. 9F).

Histological analysis of sciatic nerves revealed no significant differences in myelin anomalies among the genotypes (Fig. 4D, Supplementary Fig. 9G). However, electron microscopy images evidenced a significant decrease in nerve fibers g-ratio in *Dnm2*<sup>S619L/+</sup> and *Dnm2*<sup>K562E/+</sup> mice, correlating with a decrease in axon diameter for *Dnm2*<sup>S619L/+</sup> and *Dnm2*<sup>K562E/+</sup> together with an increase in myelin thickness for *Dnm2*<sup>K562E/+</sup> mice (Fig. 4E–G). Noteworthy, *Dnm2*<sup>S619L/K562E</sup> mice exhibited a

normalized g-ratio due to an increase of both axon diameter and myelin thickness.

### Combining CNM and CMT mutations shows long-term improvement of both phenotypes

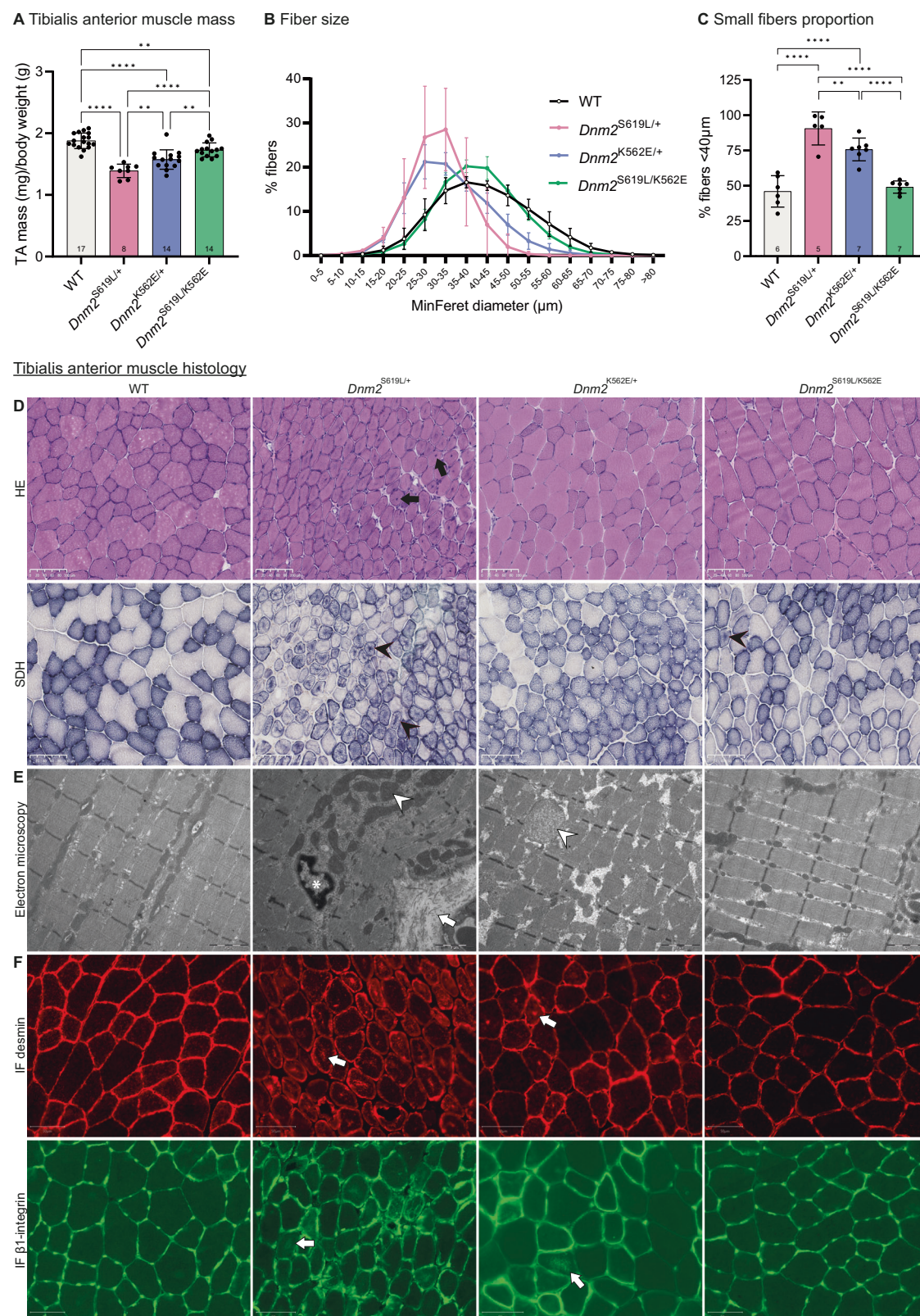
To assess the long-term effects of combining both CNM and CMT mutations, we analyzed key phenotypes in *Dnm2*<sup>S619L/K562E</sup> mice at 1 year of age. The improvements in body weight and length observed at 8 weeks were maintained at 1 year, while the hanging test was more challenging at this age due to increased fat (Fig. 5A–C). Stride was reduced in *Dnm2*<sup>S619L/+</sup> mice and rescued in *Dnm2*<sup>S619L/K562E</sup> (Fig. 5D). Contrary to what was observed at 8 weeks, no coordination defects were seen in *Dnm2*<sup>K562E/+</sup> mice at 1 year (Fig. 5D, E). Rear activity was significantly decreased at 1 year in both mutants, and there was a tendency towards improvement in *Dnm2*<sup>S619L/K562E</sup> (Fig. 5F). No hindlimb claspings was observed in either single mutant group during tail suspension (Supplementary Fig. 10A). Sensory tests revealed thermal, but not mechanical, sensitivity deficits which were absent in younger mice (Fig. 5G–I). In the hot plate test, both mutants showed higher withdrawal latencies, with a tendency toward improvement in *Dnm2*<sup>S619L/K562E</sup> mice. In the tail immersion test, the increased tail flick latency in *Dnm2*<sup>K562E/+</sup> mice was fully normalized in *Dnm2*<sup>S619L/K562E</sup>. X-ray images taken at 1.5 years revealed kyphosis and reduced body size in both single mutants, with a clear improvement in the *Dnm2*<sup>S619L/K562E</sup> (Fig. 5J).

At 1 year, electromyography (EMG) analysis revealed decreased compound sensorial nerve conduction velocity (csNCV) in *Dnm2*<sup>K562E/+</sup> mice, consistent with the observed reduced thermal sensitivity (Fig. 5G, H, Fig. 6A). csNCV was increased in *Dnm2*<sup>S619L/+</sup> and *Dnm2*<sup>S619L/K562E</sup> compared to *Dnm2*<sup>K562E/+</sup> and to WT. In contrast, the sensory amplitude was decreased in all *Dnm2*<sup>S619L/+</sup>, *Dnm2*<sup>K562E/+</sup> and *Dnm2*<sup>S619L/K562E</sup> groups compared to WT (Fig. 6B). The motor NCV and amplitudes were not affected in any of the groups (Fig. 6C, D, Supplementary Fig. 10B). These findings suggest that while the double mutant exhibit improvement in conduction velocity, they fail to rescue sensory amplitude deficits.

The TA muscle weakness in *Dnm2*<sup>S619L/+</sup> mice persisted at 1 year, as well as the rescue provided when combining both CNM and CMT mutations (Fig. 6E–G). Of note, *Dnm2*<sup>S619L/+</sup> mice still develop lower TA force following nerve stimulation compared to direct muscle stimulation, supporting conduction impairments (Fig. 6H).

TA muscle mass reduction in both *Dnm2*<sup>S619L/+</sup> and *Dnm2*<sup>K562E/+</sup> mice persisted in *Dnm2*<sup>S619L/K562E</sup> mice at 1 year (Fig. 7A). However, reductions in Gastrocnemius mass in *Dnm2*<sup>S619L/+</sup> and Soleus mass in *Dnm2*<sup>K562E/+</sup> mice were fully rescued in *Dnm2*<sup>S619L/K562E</sup> at 1 year (Fig. 7B, C). Despite no improvement in TA mass, myofiber hypotrophy was fully rescued in this muscle in *Dnm2*<sup>S619L/K562E</sup> mice, as shown by normalized fiber size (Fig. 7D–F).

In the peripheral nerves, the g-ratio remained decreased in *Dnm2*<sup>K562E/+</sup> mice compared to WT, due to thicker myelin (Fig. 7G–J). In contrast, *Dnm2*<sup>S619L/+</sup> mice showed an increased g-ratio compared to WT, driven by larger axons. In *Dnm2*<sup>S619L/K562E</sup>, the g-ratio was also



increased compared to *Dnm2*<sup>K562E/+</sup> mice, resulting from both an increase in axon diameter and thicker myelin.

Overall, the rescue of motor performance and muscle organization through the combination of CNM and CMT mutations was maintained at 1 year of age. In addition, several peripheral nerve defects were also improved.

## Discussion

Our in vitro and in vivo data shed light on the pathomechanism and support that *DNM2*-CNM mutations are gain-of-function while *DNM2*-CMT are loss-of-function. This aligns with previous studies showing *DNM2* overexpression in WT mice induced CNM-like phenotypes<sup>22,23</sup>, and Schwann cell-specific *DNM2* deletion led to CMT-like



**Fig. 3 | Combining CNM and CMT mutations restores muscle organization.** **A** TA mass normalized to body weight ( $8 \leq n \leq 17$ , from top to bottom, left to right  $^{**}P = 0.0026$ ,  $^{***}P = 0.0025$ ,  $^{****}P = 0.0026$ ). **B** TA fibers distribution based on their MinFeret diameter ( $n$  WT = 6,  $Dnm2^{S619L/+} = 5$ ,  $Dnm2^{K562E/+} = 7$ ,  $n$   $Dnm2^{S619L/K562E} = 7$ ). **C** Proportion of small fibers (MinFeret < 40  $\mu$ m) in TA sections ( $5 \leq n \leq 7$ ,  $^{**}P = 0.0096$ ,  $^{****}P < 0.0001$ ). **B** Each  $n$  represents a mouse, and the graph shows mean  $\pm$  SD. **A, C** Each dot represents a mouse. Values are represented as mean  $\pm$  SD. **A, C** Two-sided ANOVA test. Source data are provided as a Source Data file. **D** TA transversal sections stained with hematoxylin-eosin (HE, upper panel,  $5 \leq n \leq 7$  biologically independent samples per group) or succinate dehydrogenase (SDH,

bottom panel,  $5 \leq n \leq 7$  biologically independent samples per group). Internalized nuclei are indicated by black arrows and internalized oxidative staining by black arrowheads. Scale = 100  $\mu$ m. **E** Electron microscopy images of TA longitudinal sections ( $2 \leq n \leq 4$  biologically independent samples per group). The white arrow indicates fibrosis, arrowheads mitochondria and the asterisk mislocalized nucleus. Scale = 2  $\mu$ m. **F** Immunofluorescence (IF) labeling of desmin (upper panel) and  $\beta$ 1-integrin (lower panel) in TA transversal sections ( $4 \leq n \leq 7$  biologically independent samples per group). Arrows indicate fibers presenting an abnormal central accumulation of the staining. Scale = 50  $\mu$ m.

neuropathy<sup>24</sup>. Noteworthy, the heterozygous *Dnm2* knock-out mouse did not recapitulate the neuromuscular defects observed in *Dnm2*<sup>K562E/+</sup> mice, suggesting the CMT mutation potentially exerts a dominant negative effect alongside haploinsufficiency<sup>16,18</sup>. While alterations appeared stronger in muscle for the CNM mouse and in nerves for the CMT mouse, we found a phenotypic overlap that was also suggested in CNM and CMT patients<sup>8,25–27</sup>.

Strikingly, our study showed that the concomitant presence of the two *DNM2* mutations prevents both the similar muscle weakness and atrophy of CNM and CMT and the specific hallmarks of each disease (nerve and coordination for CMT and muscle histopathology for CNM) (Supplementary Fig. 11). This antagonistic effect is probably due to the capacity of both mutants to form hetero-oligomers.

This study reveals that two distinct disease-causing mutations within the *DNM2* gene compensate each other in vivo, leading to corrections of most phenotypes. It was known that different mutations in the same gene can cause various disorders, as for *LMNA* in muscular dystrophy, cardiomyopathy, or axonal neuropathy<sup>28</sup>, and for *RET* activating mutations in multiple endocrine neoplasia and inactivating mutations in Hirschsprung disease<sup>29</sup>. However, their combined potential antagonistic effect was not studied. Conversely, examples of epistasis exist when combining mutations in two different genes modifies disease development. A person carrying the *APOE3* R136S mutation remained protected from developing Alzheimer disease (AD) for three decades, despite having the *PSEN1*-AD-causing mutation<sup>30,31</sup>. Alpha-thalassemia linked to *HBA1-2* mutations or sickle cell anemia linked to *HBB* mutations individually protect against Plasmodium falciparum malaria, and lose their protective effect when combined<sup>32</sup>.

The inverse modulation of DNM2 activity emerges as promising therapeutic strategies to address *DNM2*-CNM and *DNM2*-CMT diseases. In *DNM2*-CNM, the pathomechanism is characterized by overactive GTPase activity. While earlier studies have established that reducing DNM2 levels can be therapeutic for *DNM2*-CNM in mice<sup>14,33,34</sup>, our study highlights that targeting the GTPase activity might be sufficient to achieve therapeutic benefit, suggesting that the development of DNM2 GTPase inhibitors represents a future avenue. In contrast, our data support *DNM2*-CMT is rather a loss-of-function. A therapeutic strategy may aim to increase DNM2 activity through the development of pharmacological compounds. Gene therapy also emerges as a potential avenue for both diseases. AAV-shRNA-based therapies have already demonstrated efficacy in reducing DNM2 levels in CNM mouse models<sup>35</sup>. For CMT, whether increasing DNM2 level would improve the disease remains to be determined. Overall, our study introduces the inhibition of DNM2 activity to rescue *DNM2*-CNM and the upregulation of DNM2 activity as a novel therapeutic prospect for *DNM2*-CMT.

## Methods

### Ethical statement

This research complies with all relevant ethical regulations. Animal care and experimentation were in accordance with French and European legislation and approved by the institutional ethical committee

Com'Eth IGBMC-ICS (Illkirch, France) under the APAFIS project numbers #33314-2021092710329260 and #34674-2022011417453821.

### Cloning, expression and purification of recombinant dynamins

The cDNAs of human ubiquitous isoform of Dynamin 2 (rDNM2-WT, rDNM2-SL or rDNM2-KE) without a tag and rDNM2-KE fused to a N-terminal 6x-His tag were cloned into pVL1392 transfer vector. The resulting plasmids were co-transfected in insect cells with AcMNPV viral DNA (Bac10:KO1629, $\Delta$ v-cath/chiA-LoxP:DsRed) linearized by Bsu36I to generate the recombinant baculoviruses as described previously<sup>36</sup>. The cDNA of rDNM2-SL fused to a N-terminal Flag tag was cloned into pKL vector and the gene of the recombinant protein was inserted into the MultiBac\_YFP viral genome. The virus generation, amplification and protein expression were performed using standardized procedures<sup>37</sup>.

For large scale production of recombinant dynamins, Sf21 insect cells (IGBMC baculovirus facility, Strasbourg, France) cultivated in the serum free Sf-900TMI medium (Gibco) were infected at a density of  $1.0 \times 10^6$  cells/mL and a multiplicity of infection of 5 with the virus stocks. Two days after infection, cells were pelleted by centrifugation ( $1000 \times g$  for 10 min) and snap-frozen for storage at  $-80^\circ\text{C}$ .

rDNM2-WT, rDNM2-SL and rDNM2-KE untagged proteins were purified with GST-SH3 of BIN1 bound to GSH-resin (GE Healthcare) as the SH3 domain captures full length dynamin 2 through a high affinity interaction with its PRD<sup>38</sup>. Purity and quality of the proteins after elution was analyzed after separation with SDS-PAGE followed by Coomassie staining.

To study the interaction of Flag-tagged-rDNM2-SL and His-tagged-rDNM2-KE mutants, the Sf21 insect cells were co-infected by baculoviruses carrying the genes encoding these proteins. For pull-down assay, the insect cells were collected 2 days after co-infection and the cell lysate was loaded on protein A Sepharose beads cross-linked with the M2 anti-Flag antibody (Sigma-Aldrich, St. Louis, USA). After overnight incubation at  $4^\circ\text{C}$ , half of beads were washed, separated by SDS-PAGE and analyzed by western blot with anti-DNM2, and HRP-conjugated anti-His or anti-Flag antibodies (Supplementary Table 1 Reagents). Enhanced chemiluminescence reagents (#32209 ThermoFisher Scientific) were employed to generate chemiluminescent signals, captured using Amersham Imager 600 (GE Healthcare Life Sciences). In parallel, bound proteins were eluted with Flag peptide and, after dialysis, incubated with Ni Sepharose® 6 Fast Flow (GE Healthcare) at  $4^\circ\text{C}$  overnight and washed. The beads were separated by SDS-PAGE and analyzed by western blot with same substrate and antibodies. The experiments were performed in technical triplicates.

### GTPase activity

The GTPase activity of rDNM2-WT, rDNM2-SL and rDNM2-KE untagged proteins were measured with malachite green colorimetric assay<sup>39</sup>. The proteins were incubated at different concentrations in the buffer 20 mM Hepes, pH7.4, 2.5 mM  $\text{Mg}^{2+}$ , with or without 2-Diacyl-sn-glycero-3-phospho-L-serine (PS, 4  $\mu\text{g/mL}$ ) for 90 min at  $37^\circ\text{C}$ . The concentration of GTP in the reaction mix was 0.5 mM in basal conditions (without PS) and 0.3 mM in PS-supplemented

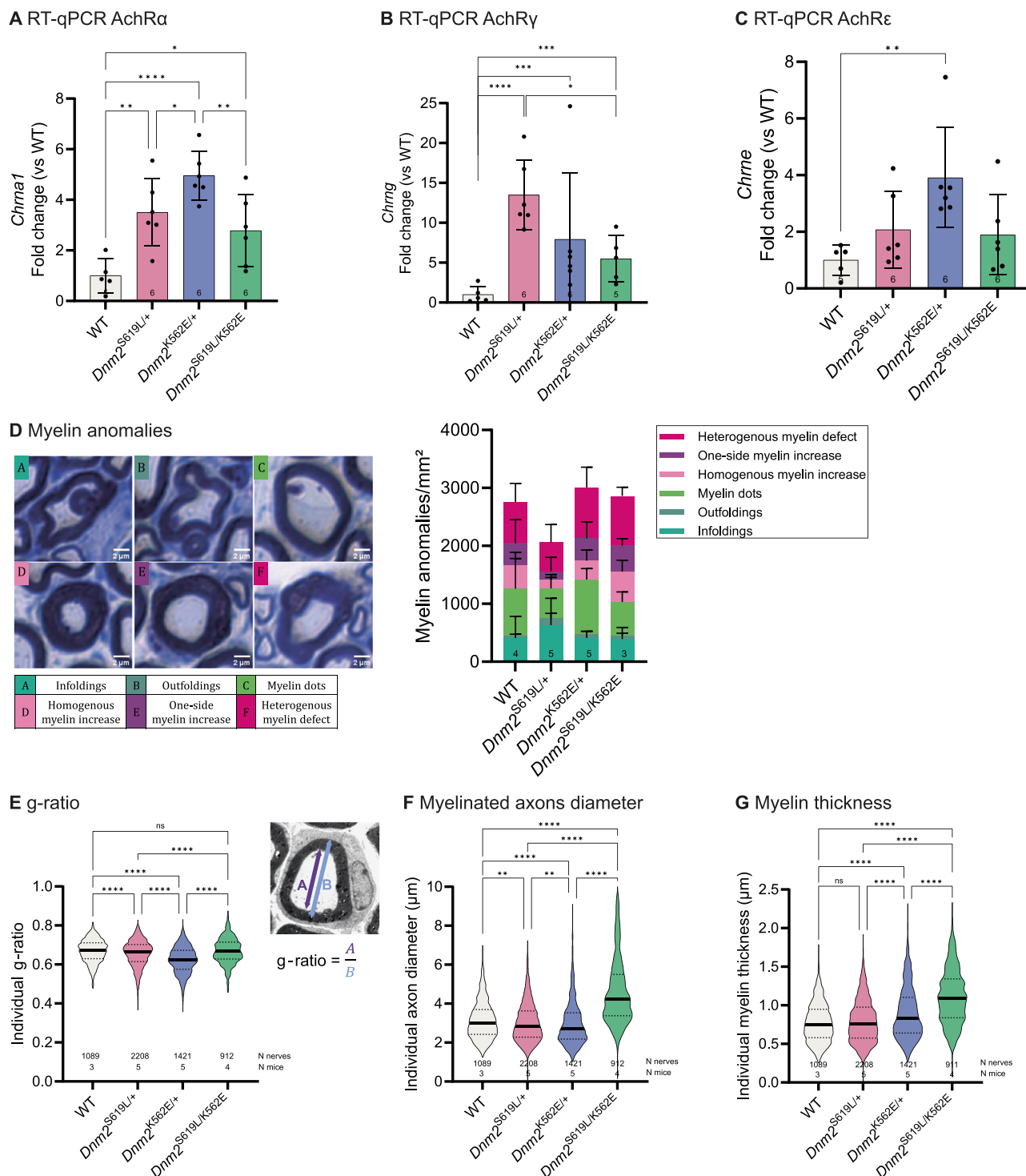


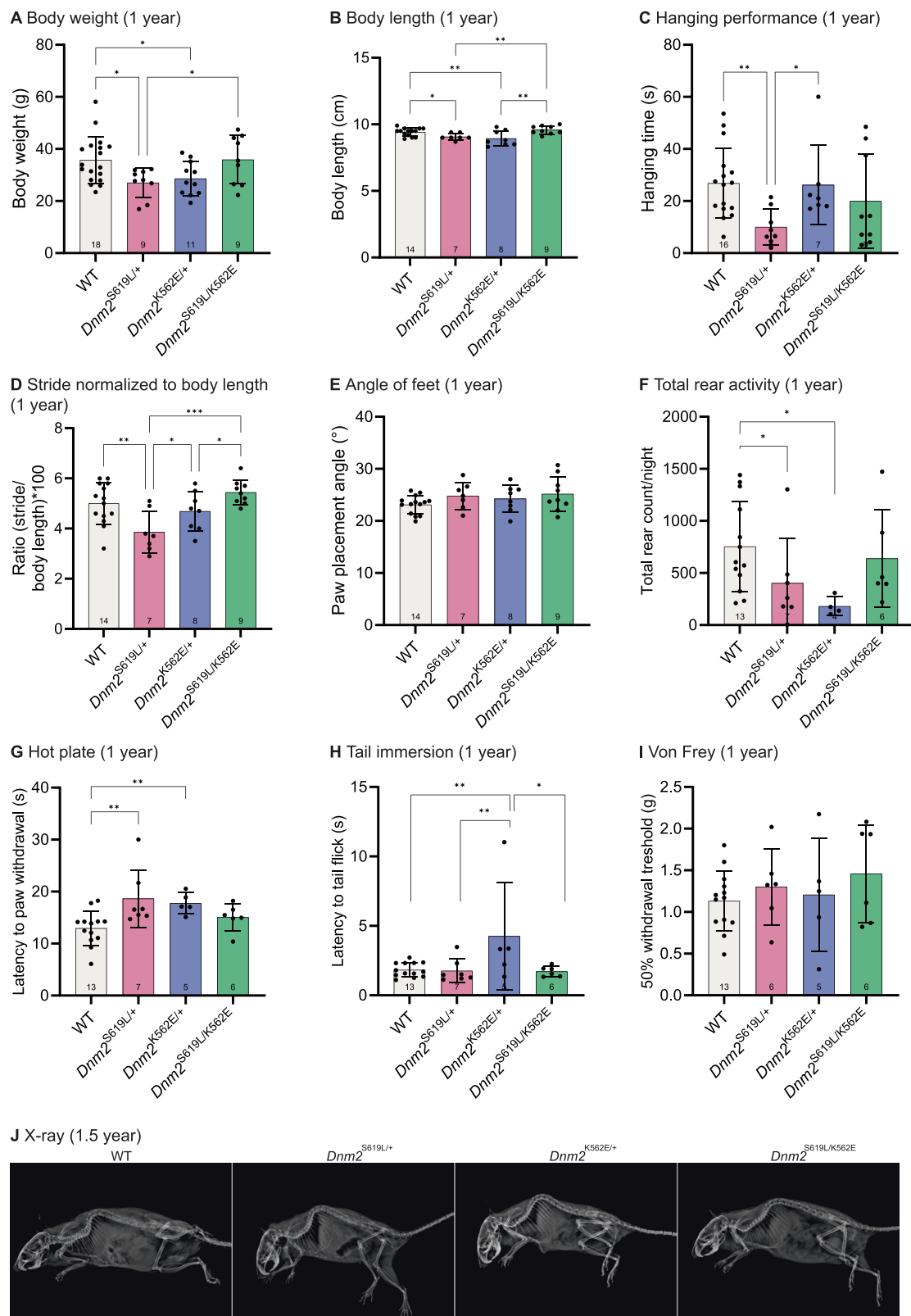
**Fig. 4 | Combining CNM and CMT mutations improves peripheral nerve defects.** **A–C** RT-qPCR analysis of acetylcholine receptor (AchR) subunits, **(A)** *Chnra1* (from top to bottom, left to right  $P=0.0199$ ,  $^{***}P<0.0001$ ,  $^{***}P=0.0021$ ,  $^{*}P=0.0436$ ,  $^{*}P=0.0043$ ), **(B)** *Chnrg* (from left to right  $^{***}P<0.0001$ ,  $^{***}P=0.0001$ ,  $^{***}P=0.0004$ ,  $^{*}P=0.0413$ ), and **(C)** *Chrne* ( $^{*}P=0.0027$ ) in TA ( $5 \leq n \leq 6$ ). **D** Categories of myelin anomalies observed in transversal sciatic nerve sections and their quantification ( $3 \leq n \leq 5$ ). Scale = 2  $\mu\text{m}$ . **A–C** Each dot represents a mouse. Values are represented

as mean  $\pm$  SD. **E–G** Violin plots showing **(E)** g-ratio ( $= \frac{\text{axon diameter}}{\text{axon} + \text{myelin diameter}}$ ) ( $^{***}P<0.0001$ ), **(F)** axon diameter (from left to right  $^{***}P=0.0010$ ,  $^{*}P=0.0048$ ,  $^{***}P<0.0001$ ), and **(G)** myelin thickness ( $^{***}P<0.0001$ ) of sciatic nerve myelinated fibers ( $911 \leq n = \text{nerves} \leq 2208$ ,  $3 \leq n = \text{mice} \leq 5$ ). **E–G** Each fiber is plotted. **A, B, D** Two-sided ANOVA test. **C, E–G** Two-sided Kruskal-Wallis test. Source data are provided as a Source Data file.

condition. Reactions were terminated with Ethylenediaminetetraacetic acid (EDTA, pH7.4), and phosphate was detected by the addition of malachite green solution (2% w/v ammonium molybdate tetrahydrate, 0.15% w/v malachite green and 4 M HCl). For heterozygous conditions, an equal proportion of each variant contributed

to the total protein concentration. GTPase activity results were confirmed with at least two different protein productions and purifications. Absorbance at 650 nm was measured with a Synergy HTX Multimode Reader (Agilent BioTek) using software Gen5 version 2.07.





### DNM2 liposome co-sedimentation assay

Liposome preparation and composition for co-sedimentation assay was done as described by Kartik Narayan and Mark A. Lemmon<sup>40</sup>. Briefly, 1,2-Dipalmitoyl-*sn*-glycerol-3-Phosphocholine (PC; Cayman Chem #15086) only or with the phospholipid of interest (1-hexadecanoyl-2-(9Z-octadecenoyl)-*sn*-glycerol-3-phospho-L-serine (PS; Avanti Research<sup>TM</sup> #840034 P) or 1,2-di-(9Z-octadecenoyl)-*sn*-glycerol-

3-[phosphoinositol-4,5-bisphosphate] (PI(4,5)P<sub>2</sub>; Avanti Research<sup>TM</sup> #850155 P)) were mixed to a 97:3 molar ratio in 1:1 chloroform/methanol and dried with argon gas for 3 h. Next, dried liposomes were resuspended to a final concentration of 2.7 mM in Buffer A (25 mM HEPES-NaOH and 150 mM of NaCl) and incubated for 1 h at 37 °C. Finally, the mixture was sonicated until obtention of a homogenized mixture.

**Fig. 5 | Combining CNM and CMT mutations shows long-term improvement on whole-body performance.** **A** Body weight of WT, *Dnm2*<sup>S619L/+</sup>, *Dnm2*<sup>K562E/+</sup> and *Dnm2*<sup>S619L/K562E</sup> mice at 1 year ( $9 \leq n \leq 18$ ), (from top to bottom, left to right  $P = 0.0356$ ,  $P = 0.0262$ ,  $P = 0.041$ ). **B** Body length measured with gait analysis. Measurement from the nose of the animal to the start of the tail ( $7 \leq n \leq 14$ ), (from left to right  $P = 0.0470$ ,  $P = 0.0065$ ,  $P = 0.0097$ ,  $P = 0.0012$ ). **C** Hanging test performance. Maximum hanging time = 60 s; WT do not reach this limit due to increased fat at this age ( $7 \leq n \leq 16$ ,  $P = 0.0041$ ,  $P = 0.0191$ ). **D** Stride (= length of a step) during treadmill walking normalized to body length ( $7 \leq n \leq 14$ , from left to right  $P = 0.0024$ ,  $P = 0.0002$ ,  $P = 0.0407$ ,  $P = 0.0465$ ). **E** Angle of feet between

paw and body line during treadmill walking ( $7 \leq n \leq 14$ ). **F** Total rear activity during the night ( $4 \leq n \leq 13$ , from left to right  $P = 0.0187$ ,  $P = 0.0251$ ). **G** Hot plate test ( $52^\circ\text{C}$ ) at 1 year. Reaction latency is recorded ( $5 \leq n \leq 13$ , from left to right  $P = 0.0046$ ,  $P = 0.0029$ ). **H** Tail immersion test ( $48^\circ\text{C}$ ) at 1 year. Reaction latency is recorded ( $5 \leq n \leq 13$ , from left to right  $P = 0.0091$ ,  $P = 0.0082$ ,  $P = 0.0139$ ). **I** Von Frey test at 1 year. Reaction to mechanic stimuli is recorded. The data presents the gram value at which the mouse is predicted to react 50% of the time ( $5 \leq n \leq 13$ ). **J** X-ray images of one mouse per genotype at 1.5 year. **A–I** Each dot represents a mouse. Values are represented as mean  $\pm$  SD. **B, D–F, H, I** Two-sided ANOVA test. **A, C, G** Two-sided Kruskal-Wallis test. Source data are provided as a Source Data file.

Liposome co-sedimentation assay was adapted from Kenniston JA, Lemmon MA<sup>12</sup>. Five  $\mu\text{g}$  of Sf21 insect cells purified recombinant DNM2, DNM2 S619L, DNM2 K562E and co-expressed DNM2 S619L with DNM2 K562E proteins (Coexpr) were prepared in Buffer A. For the mixture condition, an equimolar mixture (Mix) of purified DNM2 S619L and DNM2 K562E in Buffer A was prepared. The different protein samples were incubated at  $25^\circ\text{C}$  for 10 min and cleared by centrifugation (170,000 g, 20 min,  $20^\circ\text{C}$ ). Cleared protein samples were mixed with 1.35 mM of the indicated liposomes (PC (100), PIP2 (97:3 PC:PIP2) or PS (97:3 PC:PS)) and incubated for 20 min at  $25^\circ\text{C}$  to allow binding. This step was followed by high-speed centrifugation at 150,000 g for 20 min at  $25^\circ\text{C}$  to separate pellet and supernatant. The pellet fraction was re-suspended in Buffer A using the same volume as the supernatant. Samples were run on SDS-PAGE 8% and western blotting was performed using an anti-DNM2 antibody (Supplementary Table 1 Reagents).

## Animals

The *Dnm2*<sup>S619L/K562E</sup> mouse line was established by crossing the knock-in *Dnm2*<sup>S619L/+</sup> mouse model with the knock-in *Dnm2*<sup>K562E/+</sup> mouse model previously described<sup>14,16</sup>. The experiments were conducted using both male and female WT, *Dnm2*<sup>S619L/+</sup>, *Dnm2*<sup>K562E/+</sup>, and *Dnm2*<sup>S619L/K562E</sup> littermates, on a mixed 50% C57BL/6 N and 50% C57BL/6 J background. Animals were housed in ventilated cages with ad libitum access to food, in temperature-controlled rooms ( $19\text{--}22^\circ\text{C}$ , 40–60% humidity) on a 12 h light/dark cycle, with 100% fresh air (15 changes/hour) and positive pressure (0.5–2.55 Pa). Breeding animals received SAFE<sup>®</sup>D03 diet and transition to SAFE<sup>®</sup>D04 after weaning. Animals were monitored weekly for health and signs of distress. Euthanasia was performed by cervical dislocation in accordance with national and European regulations.

For genotyping, primers “6115 Er KE” and “6116 Ef KE” were used to detect K562E mutation and primers “9580 Ef SL” and “9581 Er SL” to detect S619L mutation (Supplementary Table 1 Reagents).

For Sanger sequencing, primers “Mf KE” and “Mr KE” were used to amplify and sequence K562E mutation, while for S619L mutation, primers “Amplif SL for” and “Amplif SL rev” were first used to amplify the genomic DNA, and after agarose gel extraction and purification with a gel clean-up kit (#740609.50 Macherey-Nagel), the “Mf SL” primer was used to sequence.

## Mouse phenotyping

All the experiments were performed either at 8 weeks of age or between 52 and 66 weeks of age. Weekly experiments were always performed on the same day of the week, by the same examiners to avoid stress and ensure reproducibility.

Body length, stride and paw angle were assessed with gait analysis on a motorized treadmill with a camera, at a constant speed of 14 cm/s. Body length was measured nose to tail base, stride as the distance between steps normalized to body length, and paw angle as the angle between body line and paw center when in contact with the surface. Three measures were averaged for body length and stride, and six for paw angle (3/side). The actimetry test measured spontaneous

locomotor activity in mice using a closed cage equipped with infrared light beams. It tracked the number of rears and locomotor activity, recorded during the night from 7 pm to 7 am, after a period of acclimatization from 10 am to 7 pm. Activity counts were averaged over the night or plotted hourly.

Hanging test measured latency to fall on an inverted grid (maximum time = 60 s), the two highest measures out of three were averaged. Mechanical sensitivity was assessed by the Von Frey test, using calibrated filaments (0.4 g – 4 g) applied perpendicularly to the hind paw’s plantar surface, recording rapid foot lifting as a positive reaction. The 50% withdrawal threshold was determined using the up-down method described by Chaplan et al.<sup>41</sup>. Thermal nociception was assessed via the hot plate ( $52^\circ\text{C}$ ) and tail immersion ( $48^\circ\text{C}$ ) tests, recording latency to paw withdrawal/licking or tail flick. These tests were repeated three times with a 5 min interval between trials, and the average was calculated (average of the two best values for the hanging). The tail suspension test was performed on 52 week-old mice by briefly suspending them. X-ray images were taken in old mice, aged 1.5 years.

## 3D structure modelisation

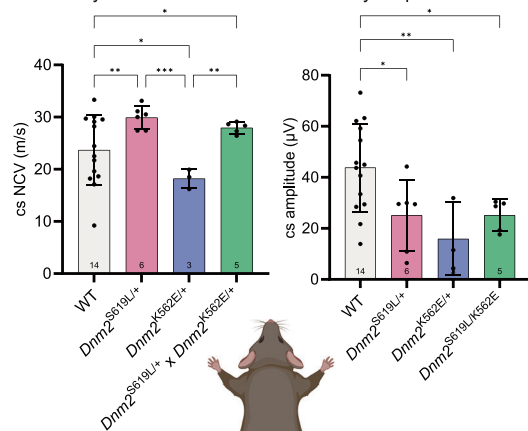
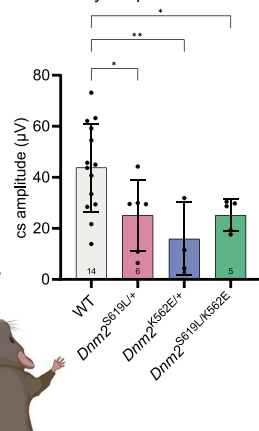
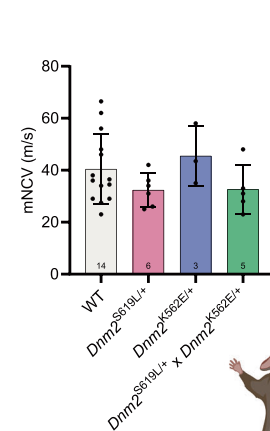
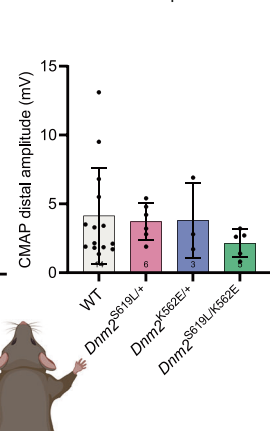
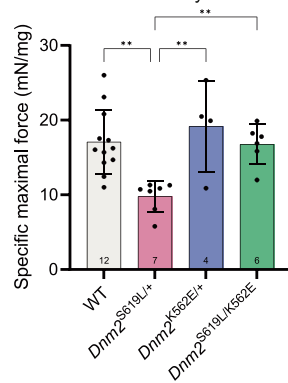
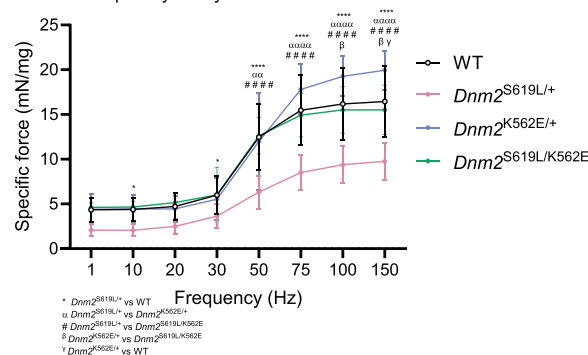
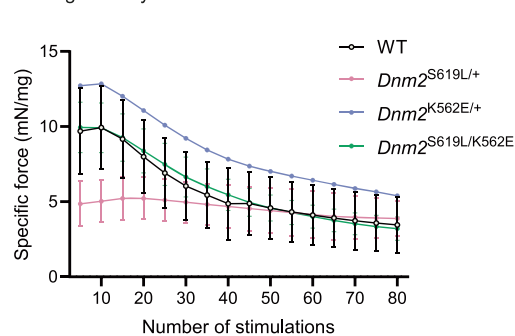
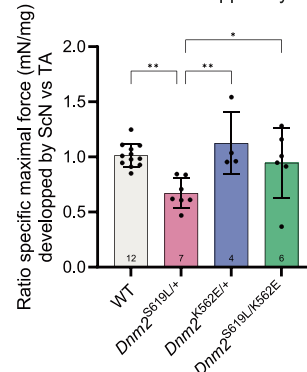
The 3D structure figure was prepared on PyMOL, using the Crystal structure of nucleotide-free human dynamin 1 (PDB identifier: 3SNH)<sup>42</sup>.

## Electrophysiology

Mice were anesthetized with isoflurane, induced at 3% and maintained at 2% in oxygen-enriched air throughout the procedure. Core body temperature was monitored using a rectal probe and maintained within the range of  $34\text{--}37^\circ\text{C}$  with the help of a heating pad. During sensitive measurements, an additional heating lamp was positioned near the tail. To prevent corneal desiccation, ocrigel was applied to the eyes. EMG recordings were performed using a Natus Mag2Health electromyograph, following standard protocols. For the measurements, the stimulating and recording electrodes were positioned as shown in Fig. 6. A needle electrode, connected to ground, was placed between the stimulation site and the recording site. For motor nerve assessments, proximal stimulation was applied to the sciatic nerve, while distal stimulation was applied at the ankle. The ground electrode was placed subcutaneously on the contralateral side, and the recording electrode was placed in the plantar muscle (Fig. 6, Supplementary Fig. 10B). 0.1 ms stimulations were delivered at various intensities, adapted to obtain maximal responses for both motor and sensory measurements.

## Muscle force measurement

In situ TA muscle contractile properties were assessed at 8 weeks by sciatic nerve and TA muscle stimulation using the Complete1300A mouse test system (Aurora Scientific). Mice were anesthetized with sequential intraperitoneal injections of domitor (2 mg/kg) and fentanyl (0.28 mg/kg), diazepam (8 mg/kg) and fentanyl (0.28 mg/kg). Mice were placed under a heating lamp. The tibialis anterior (TA) muscle was exposed by removing the skin from the lower hindlimb. An incision was made on the thigh to expose the sciatic nerve. The distal

**EMG (1 year)****A Sensory NCV****B Sensory amplitude****C Motor NCV****D Motor distal amplitude****Sensory nerve conduction assessment****Distal motor conduction assessment****In situ muscle force with TA stimulation (1 year)****E Maximal force analysis****F Force frequency analysis****G Fatigue analysis****H Maximal force developed by sciatic nerve vs TA stimulation**

tendon of the TA was detached and fixed to an isometric transducer. The limb was stabilized by clamping the knee joint and needle electrodes were inserted around the sciatic nerve. The optimal muscle length as well as the optimal stimulation intensity, at which the muscle produced the maximal isometric twitch force, were adjusted until there was no further increase in peak twitch force. First, electrodes were placed around the sciatic nerve and TA muscle force was assessed

at 150 Hz and at various incremental frequencies (1–150 Hz; 0.5 s duration, 30 s rest interval). Then, electrodes were placed directly on the TA muscle, these tests were repeated and a fatigue protocol was conducted (80 contractions of 40 Hz with 1 s on, 3 s off). For the three, the peak force of each contraction was measured. For the fatigue protocol, the tetanic force was averaged every five contractions for clarity, and the drop in force was calculated as the percentage decrease



**Fig. 6 | Combining CNM and CMT mutations shows long-term improvement on neuromuscular function.** **A, B** Sensory electrophysiology: **(A)** compound sensory nerve conduction velocity (csNCV) (from top to bottom, left to right  $P=0.0358$ ,  $P=0.0212$ ,  $P=0.0062$ ,  $P=0.0005$ ,  $P=0.0044$ ), and **(B)** cs amplitude ( $3 \leq n \leq 14$ , from left to right  $P=0.0171$ ,  $P=0.0074$ ,  $P=0.0250$ ). **C, D** Motor electrophysiology: **(C)** motor NCV, and **(D)** compound muscle action potential (CMAP) amplitude, measured distally as illustrated ( $3 \leq n \leq 14$ ). Stim = stimulation, Rec = recording electrodes. Created in BioRender. Laporte, J. (2025) <https://BioRender.com/sk689pl>. **E** Maximal force developed by TA muscle when stimulating the TA at 150 Hz, normalized to TA mass ( $4 \leq n \leq 12$ , from left to right  $P=0.0013$ ,  $P=0.0024$ ,  $P=0.0041$ ). **F** Force developed by TA muscle when stimulating the TA at different incremental frequencies (1–150 Hz), normalized to TA mass ( $n$  WT = 12,  $Dnm2^{S619L/+} = 7$ ,  $Dnm2^{K562E/+} = 3$ ,  $Dnm2^{S619L/K562E} = 6$ , from left to right  $P=0.05$ ,

$P=0.0479$ ,  $\alpha P=0.0012$ ,  $\beta P=0.0345$ ,  $\beta P=0.0127$ ,  $\gamma P=0.0303$ ,  $\alpha\alpha\alpha\alpha/####P<0.0001$ ). **G** Force developed by TA muscle over 80 consecutive TA stimulations at 40 Hz, normalized to TA mass ( $n$  WT = 10,  $Dnm2^{S619L/+} = 7$ ,  $Dnm2^{K562E/+} = 1$ ,  $Dnm2^{S619L/K562E} = 6$ ). **H** Ratio of the maximal force developed from sciatic nerve vs. TA muscle stimulation ( $4 \leq n \leq 12$ , from left to right  $P=0.0011$ ,  $P=0.0037$ ,  $P=0.0152$ ). **F, G** Each  $n$  represents a mouse, and the graphs show mean  $\pm$  SD. **A–E** and **H** Each dot represents a mouse. Values are represented as mean  $\pm$  SD. In **(F, G)** significant differences between  $Dnm2^{S619L/+}$  and WT,  $Dnm2^{K562E/+}$  or  $Dnm2^{S619L/K562E}$  groups were indicated with \*,  $\alpha$ , and # respectively. While  $\gamma$  and  $\beta$  shows differences between  $Dnm2^{K562E/+}$  and WT or  $Dnm2^{S619L/K562E}$  respectively. **A–D**, and **F, G** Two-sided ANOVA test. **E, H** Two-sided Kruskal-Wallis test. Source data are provided as a Source Data file.

in force from the first 5 to the last 5 stimulations. In the graphs, the specific force (in mN/mg) was obtained by normalizing the force to TA muscle mass.

### Tissue collection

After the muscle force measurement, mice were euthanized by cervical dislocation and muscles were weighted and collected. TA was frozen in liquid nitrogen-cooled isopentane and stored at  $-80^{\circ}\text{C}$  for later histology, RNA and protein extraction. Sciatic nerves used for molecular analyzes were snap-frozen in liquid nitrogen and stored at  $-80^{\circ}\text{C}$ . TA and sciatic nerve used for electron microscopy were fixed in 2.5% glutaraldehyde + 2.5% PFA and stored at  $4^{\circ}\text{C}$ .

### Muscle histology

$8\mu\text{m}$  transversal muscle sections were stained with HE, SDH, or aspecific esterase and imaged using the NanoZoomer 2.0-HT slide scanner (Hamamatsu Photonics). 20X images were used for analysis. Fiber size distribution, circularity and nuclei counting were determined on TA sections stained with HE, using CellPose software<sup>43</sup> to segment individual fibers and using Fiji<sup>44</sup> to calculate fibers MinFerret diameter and circularity. For the circularity, fibers were classified from 0 to 1, 0 corresponding to a line and 1 to a circle. Nuclei and SDH internalization were counted manually using QuPath software<sup>45</sup>. One transversal section of the whole muscle was quantified for each animal.

### Immunofluorescence

$8\mu\text{m}$  transversal muscle sections were fixed 20 min with paraformaldehyde 4%, permeabilized 10 min with PBS-Triton X100 0.2% (#T8787-250ML Merck), blocked 1 h with PBS-Triton X100 0.1% + 5% BSA (#02160069-CF MP Bio) and immunostained overnight at  $4^{\circ}\text{C}$  using the primaries anti-integrin- $\beta 1$  and anti-desmin antibodies or the primary anti-collagen VI antibody (Supplementary Table 1 Reagents). The Alexa-coupled secondary antibodies were incubated together with the DAPI for 1 h at room temperature. Slides were mounted in ProLong Gold Antifade media (#P36934 ThermoFisher Scientific). 20X images were acquired using the Zeiss Axio Observer 7 microscope. A section without primary antibody was used for each animal as a negative control. For integrin and desmin analysis, fibers were segmented with CellPose and classified with QuPath as positive or negative based on the mean staining intensity within each fiber. A consistent threshold was used across all animals. The percentage of positive fibers per section is presented. For collagen VI, the staining thickness was quantified on Fiji using the line tool. Around 50 interfibers per mouse section were quantified, with 6 mice per genotype.

### Electron microscopy

The TA and sciatic nerves samples were fixed by immersion in 2.5% glutaraldehyde and 2.5% paraformaldehyde in cacodylate buffer (0.1M, pH 7.4), and washed in cacodylate buffer for further 30 min. The samples were postfixed in 1% osmium tetroxide in 0.1M cacodylate buffer for 1 h at  $4^{\circ}\text{C}$  and dehydrated through graded alcohol (50,

70, 90, and 100%) and propylene oxide for 30 min each. Samples were oriented (TA longitudinal, nerve transversal) and embedded in Epon 812. For sciatic nerves only, semithin sections were cut at  $2\mu\text{m}$  for further histological analyses. For both muscle and nerve, ultrathin sections were cut at 70 nm (Leica Ultracut UCT) and contrasted with uranyl acetate and lead citrate and examined at 70 kv with a Morgagni 268D electron microscope (FEI Electron Optics, Eindhoven, the Netherlands) equipped with a Mega View III camera (Soft Imaging System) or with a Philips CM12 electron microscope equipped with a Gatan OneView Camera (Gatan). Sciatic nerves sections were made consistently at the distal extremity.

Z-line misalignment in EM images was quantified using the angle tool in Fiji, as described in Supplementary Fig. 8A, from 2–4 mice per genotype and at least 220 sarcomeres. Mitochondrial area and circularity were assessed in QuPath via manual segmentation and annotation measurements, with 2–4 mice per genotype and at least 100 mitochondria analyzed.

### Sciatic nerve histology

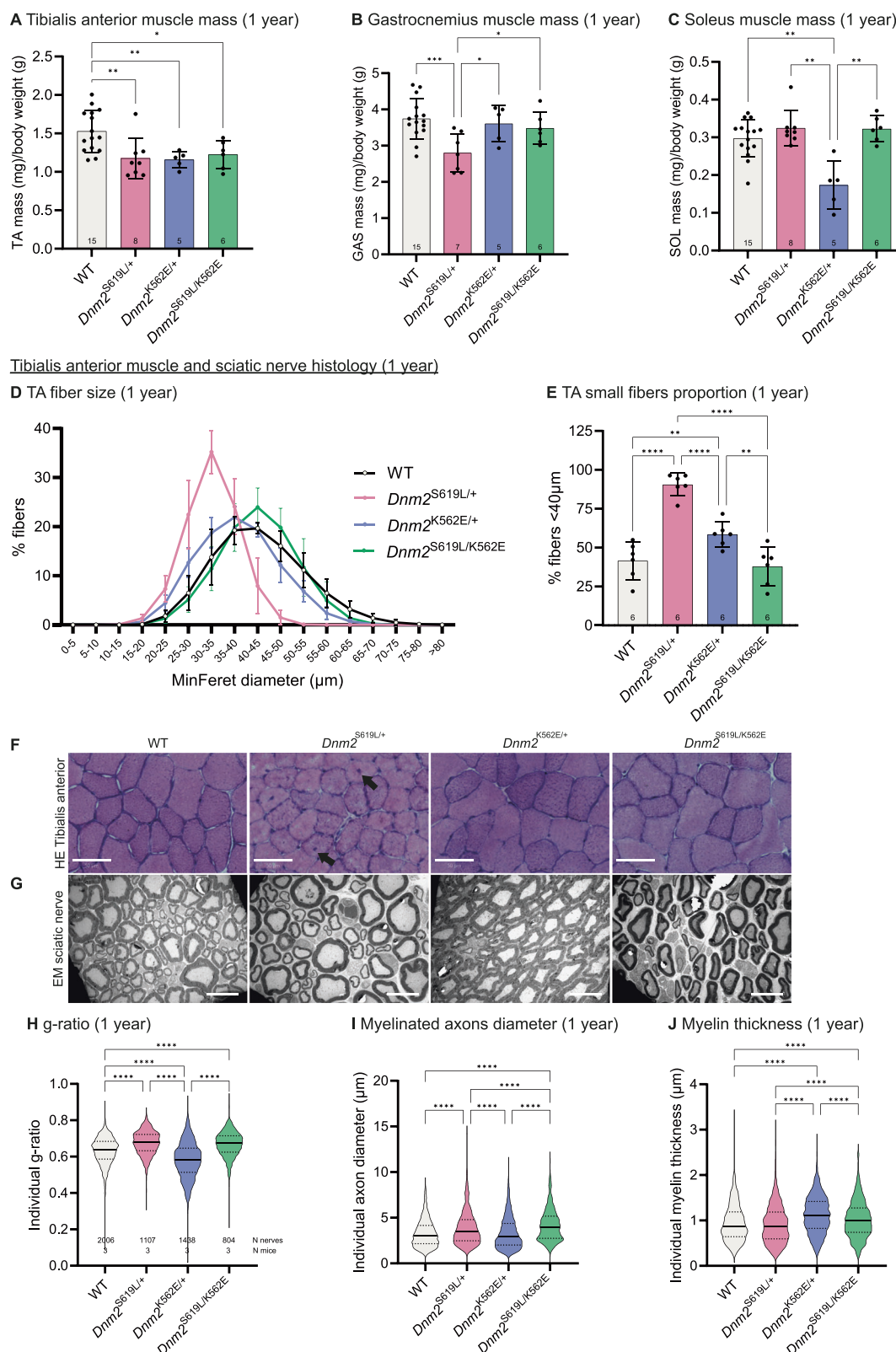
Semithin transversal sections, mentioned above, were stained with Toluidine Blue and 63X images were acquired using the Zeiss Axio Observer 7 microscope. For each animal, myelin anomalies were assessed manually in an entire nerve section with QuPath. g-ratio, axon diameter and myelin thickness measurements were performed using for each nerve a set of 10 electron microscopy images, covering different regions of the nerve, captured at a  $10\mu\text{m}$  scale and the Axon-DeepSeg segmentation software<sup>46</sup>.

### RNA extraction and qRT-PCR

RNA was isolated from TA muscle samples using TRI Reagent (#TR118 Molecular Research Center) and the Precellys® Evolution Touch tissue homogenizer (Bertin technologies) (2x15s cycles at 5500 rpm). cDNA synthesis was achieved using SuperScriptIV Reverse Transcriptase (#18090010 Invitrogen). qPCR was done with cDNA amplified and SYBER Green Master Mix I (#04887352001 Roche Diagnostics) together with  $0.5\mu\text{M}$  of forward and reverse primers (Supplementary Table 1 Reagents). qRT-PCR was performed using technical triplicates. Amplicons were analyzed using a Lightcycler 480 (Roche Diagnostics). The expression level of each transcript was expressed relative to that of the housekeeping gene *Rsp11* using the  $2^{(-\Delta\Delta\text{Ct})}$  method and expressed as the fold change from the average of the WT control group.

### RT-ddPCR

RNA was extracted from TA muscles at 8 weeks as described above. The RT-ddPCR was performed at the ICS as previously described<sup>47</sup>. The RT-ddPCR used FAM or HEX reporter dyes and ZEN/Iowa Black FQ double-quenched nuclease probes (IDT, Coralville, IA, USA) either targeting the WT or mutated forms of *Dnm2* (Supplementary Table 1 Reagents). The reactions were conducted in a QX200 Droplet Digital PCR System (Bio-Rad, Hercules, CA, USA). Data were normalized to the reference gene *Hprt* and to mean value of control group (set to 100%).



### Protein extraction

TA muscles and sciatic nerves samples were placed in RIPA buffer supplemented with PMSF 1 mM, Sodium Orthovanadate 1 mM, Sodium Fluoride 5 mM, and Protease Inhibitor Cocktail 1X. Tissue samples were lysed using Precellys® Evolution Touch tissue homogenizer (Bertin technologies) (2x 20 s cycles at 6000 rpm) and cleared by

centrifugation. Protein concentrations were quantified using a DC Protein Assay Kit (#5000116 BioRad).

### Western blot

Extracted protein were separated using a polyacrylamide gel, prepared with the TGX™ FastCast™ Acrylamide Kit (#1610173 BioRad). A 10% gel

**Fig. 7 | Combining CNM and CMT mutations shows long-term improvement on muscle and nerve structure.** **A–C** Muscle mass of **(A)** TA (from left to right  $^{**}P=0.0013$ ,  $^{*}P=0.0053$ ,  $^{*}P=0.0138$ ), **(B)** Gastrocnemius (from left to right  $^{**}P=0.0005$ ,  $^{*}P=0.0137$ ,  $^{*}P=0.0271$ ), and **(C)** Soleus (from left to right  $^{**}P=0.0073$ ,  $^{*}P=0.0021$ ,  $^{*}P=0.0020$ ), normalized to body weight at 1 year ( $5 \leq n \leq 15$ ). **D** TA fibers distribution based on their MinFerret diameter ( $n=6$ ). **E** Proportion of small fibers (MinFerret  $< 40 \mu\text{m}$ ) in TA sections ( $n=6$ , from left to right  $^{**}P=0.0097$ ,  $^{*}P=0.0025$ ,  $^{***}P<0.0001$ ). **D** Each  $n$  represents a mouse, and the graph shows mean  $\pm$  SD. **A–C, E** Each dot represents a mouse. Values are represented as

mean  $\pm$  SD. **F** TA transversal sections stained with hematoxylin-eosin (HE, upper panel,  $n=6$  biologically independent samples per group). Internalized nuclei are indicated by black arrows. Scale =  $50 \mu\text{m}$ . **G** Electron microscopy images of sciatic nerve transversal sections (lower panel,  $n=3$  biologically independent samples per group). Scale bar =  $10 \mu\text{m}$ . **H–J** Violin plots showing **(H)** g-ratio ( $= \frac{\text{axon diameter}}{\text{axon} + \text{myelin diameter}}$ ), **(I)** axon diameter, and **(J)** myelin thickness of sciatic nerve myelinated fibers ( $804 \leq n = \text{nerves} \leq 2006$ ,  $n = \text{mice} = 3$ ,  $^{***}P<0.0001$ ). **H–J** Each fiber is plotted. **A, B, E** Two-sided ANOVA test. **C, H–J** Two-sided Kruskal–Wallis test. Source data are provided as a Source Data file.

was used for most antigen detection, with the exception of LC3B and cytC for which a 15% gel was manually prepared.  $10 \mu\text{g}$  of protein in a volume of  $12 \mu\text{L}$  was loaded for TA muscle samples, while  $5 \mu\text{g}$  of protein in a volume of  $20 \mu\text{L}$  was loaded for sciatic nerve samples. Electrophoretic migration was conducted at  $200 \text{ V}$  for  $\sim 30 \text{ min}$ . Protein transfer to nitrocellulose membranes was carried out for  $5\text{--}10 \text{ min}$  at  $2.5 \text{ A}$  using the Trans-Blot Turbo RTA Mini Nitrocellulose Transfer Kit (#170-4270 BioRad). Ponceau S staining was performed. Membranes were blocked for  $1 \text{ h}$  in TBS containing 5% nonfat dry milk and 0.1% Tween-20 (TBST) (#P2287-500ML Merck) before overnight  $4^\circ\text{C}$  incubation with a specific primary antibody (Supplementary Table 1 Reagents) diluted in 5% nonfat dry milk in TBST (except p-S6RP and S6RP antibodies that were diluted in 5% BSA in TBST). Membranes were washed and incubated with appropriate HRP-conjugated secondary antibodies for  $1 \text{ h}$  at room temperature. Enhanced chemiluminescence reagents (#32209 ThermoFisher Scientific) were employed to generate chemiluminescent signals, captured using Amersham Imager 600 (GE Healthcare Life Sciences). Fiji was used to quantify bands intensity. Data were normalized to ponceau staining and the mean value of control group, except desmin that was normalized to GAPDH instead of the ponceau for practical reasons.

To detect p-S6RP and total S6RP, a single membrane was initially probed with the anti-phospho antibody for p-S6RP. After signal detection, the membrane underwent a  $45 \text{ min}$  stripping procedure using Western ReProbe™ PLUS media (#786-307 G-Biosciences). The western procedure was started again, from ponceau S staining, using the primary anti-S6RP antibody to detect the total form. Each form was first normalized to its ponceau and then the phosphorylated form was normalized to the total one.

All unedited western blots used for protein quantification, including those not shown in the figures and their loading controls, are provided in Supplementary Fig. 12.

### Statistical analyses

Statistical analyses and graphs were made using GraphPad Prism version 9.5.1. Initially, a two-way ANOVA was performed for most experiments to assess the effects of sex and genotype. This analysis revealed significant effects of the genotype on most phenotypes. In some phenotypes (e.g. body weight and length), both genotype and sex impacted the measures; however, there was no significant interaction between these two factors, indicating that the genotype differences were consistent across both sexes (Supplementary Fig. 10C, D). Subsequently, to consolidate the findings, data from males and females were combined. The number of males and females used in each test is available (Supplementary Data 1 Statistics).

The normality of data distribution was assessed using the Shapiro-Wilk test, except when the sample size was large, in which case the D'Agostino & Pearson test was used. If all data followed a normal distribution, a one-way ANOVA was performed. Alternatively, a Brown-Forsythe and Welch ANOVA was employed if the assumption of equal variances was violated. When data were lognormal rather than normal, a log transformation was performed before ANOVA analysis. For data not following a normal or lognormal distribution, a Kruskal–Wallis test was performed. Multiple comparisons of normally distributed data

with homoscedastic or heteroscedastic variances were conducted using uncorrected Fischer's LSD test and unpaired  $t$ -test with Welch's correction, respectively. For non-normally distributed data, an uncorrected Dunn's test was used. When a data point visually deviated from a dataset, the ROUT outlier test was conducted (with the strictest threshold of  $Q=0.1\%$ ), and if an outlier was detected, it was subsequently removed from the dataset and the graph. Details of each test performed are summarized in Supplementary Data 1.  $p<0.05$  was considered statistically significant. For all graphs, all pairwise comparisons were performed, and only significant differences were plotted (except Fig. 1E). Graphs show individual data points, and mean  $\pm$  SD.

### Study approval

Animal care and experimentation were in accordance with French and European legislation and approved by the institutional ethical committee Com'Eth IGBMC-ICS (Illkirch, France) under the APAFIS project numbers #33314-2021092710329260 and #34674-2022011417453821. This study complies with the ARRIVE guidelines for reporting animal experiments.

### Reporting summary

Further information on research design is available in the Nature Portfolio Reporting Summary linked to this article.

### Data availability

Source data are provided with this paper. All data necessary to reproduce the findings of this work will be shared by the corresponding author upon request. Source data are provided with this paper.

### References

1. Praefcke, G. J. K. & McMahon, H. T. The dynamin superfamily: universal membrane tubulation and fission molecules? *Nat. Rev. Mol. Cell Biol.* **5**, 133–147 (2004).
2. Antonny, B. et al. Membrane fission by dynamin: what we know and what we need to know. *EMBO J.* **35**, 2270–2284 (2016).
3. Laiman, J., Lin, S.-S. & Liu, Y.-W. Dynamins in human diseases: differential requirement of dynamin activity in distinct tissues. *Curr. Opin. Cell Biol.* **81**, 102174 (2023).
4. Reubold, T. F. et al. Crystal structure of the dynamin tetramer. *Nature* **525**, 404–408 (2015).
5. Bitoun, M. et al. Mutations in dynamin 2 cause dominant centronuclear myopathy. *Nat. Genet.* **37**, 1207–1209 (2005).
6. Züchner, S. et al. Mutations in the pleckstrin homology domain of dynamin 2 cause dominant intermediate Charcot-Marie-tooth disease. *Nat. Genet.* **37**, 289–294 (2005).
7. Durieux, A.-C., Prudhon, B., Guicheney, P. & Bitoun, M. Dynamin 2 and human diseases. *J. Mol. Med.* **88**, 339–350 (2010).
8. Böhm, J. et al. Mutation spectrum in the large GTPase dynamin 2, and genotype-phenotype correlation in autosomal dominant centronuclear myopathy. *Hum. Mutat.* **33**, 949–959 (2012).
9. Bitoun, M. et al. Dynamin 2 mutations cause sporadic centronuclear myopathy with neonatal onset. *Ann. Neurol.* **62**, 666–670 (2007).



10. Srinivasan, S., Dharmarajan, V., Reed, D. K., Griffin, P. R. & Schmid, S. L. Identification and function of conformational dynamics in the multidomain GTPase dynamin. *EMBO J.* **35**, 443–457 (2016).
11. Chin, Y.-H. et al. Dynamin-2 mutations associated with centronuclear myopathy are hypermorphic and lead to T-tubule fragmentation. *Hum. Mol. Genet.* **24**, 5542–5554 (2015).
12. Kenniston, J. A. & Lemmon, M. A. Dynamin GTPase regulation is altered by PH domain mutations found in centronuclear myopathy patients. *EMBO J.* **29**, 3054–3067 (2010).
13. Wang, L. et al. Dynamin 2 mutants linked to centronuclear myopathies form abnormally stable polymers. *J. Biol. Chem.* **285**, 22753–22757 (2010).
14. Muñoz, X. M. et al. Physiological impact and disease reversion for the severe form of centronuclear myopathy linked to dynamin. *JCI Insight* **5**, e137899 (2020).
15. Stavrou, M., Sargiannidou, I., Christofi, T. & Kleopa, K. A. Genetic mechanisms of peripheral nerve disease. *Neurosci. Lett.* **742**, 135357 (2021).
16. Pereira, J. A. et al. Mice carrying an analogous heterozygous dynamin 2 K562E mutation that causes neuropathy in humans develop predominant characteristics of a primary myopathy. *Hum. Mol. Genet.* **29**, 1253–1273 (2020).
17. Ferguson, S. et al. Coordinated actions of actin and BAR proteins upstream of dynamin at endocytic clathrin-coated pits. *Dev. Cell* **17**, 811–822 (2009).
18. Cowling, B. S. et al. Reducing dynamin 2 expression rescues X-linked centronuclear myopathy. *J. Clin. Invest.* **124**, 1350–1363 (2014).
19. Sartori, R., Romanello, V. & Sandri, M. Mechanisms of muscle atrophy and hypertrophy: implications in health and disease. *Nat. Commun.* **12**, 330 (2021).
20. Moreno-Layseca, P., Icha, J., Hamidi, H. & Ivaska, J. Integrin trafficking in cells and tissues. *Nat. Cell Biol.* **21**, 122–132 (2019).
21. Liao, Z. et al. CHRNA1 induces sarcopenia through neuromuscular synaptic elimination. *Exp. Gerontol.* **166**, 111891 (2022).
22. Liu, N. et al. Mice lacking microRNA 133a develop dynamin 2-dependent centronuclear myopathy. *J. Clin. Invest.* **121**, 3258–3268 (2011).
23. Cowling, B. S. et al. Increased expression of wild-type or a centronuclear myopathy mutant of dynamin 2 in skeletal muscle of adult mice leads to structural defects and muscle weakness. *The Am. J. Pathol.* **178**, 2224–2235 (2011).
24. Gerber, D. et al. Schwann cells, but not Oligodendrocytes, depend strictly on dynamin 2 function. *eLife* **8**, e42404 (2019).
25. Castillo-Ferrán, N. et al. A possible case of centronuclear myopathy: a case report. *Medicina* **59**, 1112 (2023).
26. Echaniz-Laguna, A. et al. Subtle central and peripheral nervous system abnormalities in a family with centronuclear myopathy and a novel dynamin 2 gene mutation. *Neuromuscul. Dis.* **17**, 955–959 (2007).
27. Saif, H. et al. A unique patient with DNM2 related peripheral neuropathy with myopathy. In *Association of British Neurologists: Annual Meeting Abstracts 2023 A88.2-A88*, 94 (BMJ Publishing Group Ltd, 2023).
28. Worman, H. J. & Bonne, G. “Laminopathies”: A wide spectrum of human diseases. *Exp. Cell Res.* **313**, 2121–2133 (2007).
29. Nakatani, T. et al. Point mutagenesis in mouse reveals contrasting pathogenetic effects between MEN2B- and Hirschsprung disease-associated missense mutations of the *RET* gene. *Dev. Growth Differ.* **62**, 214–222 (2020).
30. Zalusky, K. A., Nelson, M. R. & Huang, Y. An Alzheimer’s-disease-protective APOE mutation. *Nat. Med.* **25**, 1648–1649 (2019).
31. Arboleda-Velasquez, J. F. et al. Resistance to autosomal dominant Alzheimer’s disease in an APOE3 Christchurch homozygote: a case report. *Nat. Med.* **25**, 1680–1683 (2019).
32. Williams, T. N. et al. Negative epistasis between the malaria-protective effects of  $\alpha$ -thalassemia and the sickle cell trait. *Nat. Genet.* **37**, 1253–1257 (2005).
33. Buono, S. et al. Reducing dynamin 2 (DNM2) rescues DNM2-related dominant centronuclear myopathy. *Proc. Natl. Acad. Sci. USA* **115**, 11066–11071 (2018).
34. de Carvalho Neves, J., Moschovaki-Filippidou, F., Böhm, J. & Laporte, J. DNM2 levels normalization improves muscle phenotypes of a novel mouse model for moderate centronuclear myopathy. *Mol. Ther. Nucleic Acids* **33**, 321–334 (2023).
35. Tasfaout, H. et al. Single intramuscular injection of AAV-shRNA reduces DNM2 and prevents myotubular myopathy in mice. *Mol. Ther.* **26**, 1082–1092 (2018).
36. Njume, F. N. et al. Identification and characterization of the *Onchocerca volvulus* excretory secretory product Ov28CRP, a putative GM2 activator protein. *PLoS Negl. Trop. Dis.* **13**, e0007591 (2019).
37. Vijayachandran, L. S. et al. Gene gymnastics: synthetic biology for baculovirus expression vector system engineering. *Bioengineered* **4**, 279–287 (2013).
38. Gómez-Oca, R. et al. Differential impact of ubiquitous and muscle dynamin 2 isoforms in muscle physiology and centronuclear myopathy. *Nat. Commun.* **13**, 6849 (2022).
39. Quan, A. & Robinson, P. J. Rapid purification of native dynamin I and colorimetric GTPase assay. *Methods Enzymol.* **404**, 556–569 (2005).
40. Narayan, K. & Lemmon, M. A. Determining selectivity of phosphoinositide-binding domains. *Methods* **39**, 122–133 (2006).
41. Chaplan, S. R., Bach, F. W., Pogrel, J. W., Chung, J. M. & Yaksh, T. L. Quantitative assessment of tactile allodynia in the rat paw. *J. Neurosci. Methods* **53**, 55–63 (1994).
42. Faelber, K. et al. Crystal structure of nucleotide-free dynamin. *Nature* **477**, 556–560 (2011).
43. Stringer, C., Wang, T., Michaelos, M. & Pachitariu, M. Cellpose: a generalist algorithm for cellular segmentation. *Nat. Methods* **18**, 100–106 (2021).
44. Schindelin, J. et al. Fiji: an open-source platform for biological-image analysis. *Nat. Methods* **9**, 676–682 (2012).
45. Bankhead, P. et al. QuPath: Open source software for digital pathology image analysis. *Sci. Rep.* **7**, 16878 (2017).
46. Zaimi, A. et al. AxonDeepSeg: automatic axon and myelin segmentation from microscopy data using convolutional neural networks. *Sci. Rep.* **8**, 3816 (2018).
47. Lindner, L. et al. Reliable and robust droplet digital PCR (ddPCR) and RT-ddPCR protocols for mouse studies. *Methods* **191**, 95–106 (2021).

## Acknowledgements

The authors would like to thank Ueli Suter and the Mouse Clinical Institute (ICS, Illkirch) for providing the *Dnm2*<sup>K562E/+</sup> mouse. We acknowledge the support of the scientific platforms at the Institut de Génétique et de Biologie Moléculaire et Cellulaire (IGBMC), particularly Nadia Messaddeq and Chadia Nahy for electron microscopy preparation and imaging, and Loïc Lindner and Pauline Cayrou for ddPCR reactions. We also thank Frédérique René for her assistance with the analysis of sciatic nerve sections, and Xènia Massana-Muñoz and Luc Dupuis for discussions. This work of the Interdisciplinary Thematic Institute IMCBio, as part of the ITI 2021-2028 program of the University of Strasbourg, CNRS and Inserm, was supported by IdEx Unistra (ANR-10-IDEX-0002), and by SFRI-STRAT’US project (ANR-20-SFRI-0012) and EUR IMCBio (ANR-17-EURE-0023) under the framework of the French Investments for the Future Program, and by ANR Dynather (ANR-18-CE17-0006-02). We acknowledge the IGBMC imaging center, member of the national infrastructure France-BioImaging supported by the French National Research Agency (ANR-10-INBS-04). SF was supported by CNRS and AFM-Téléthon. PAP received a CONACYT Campus France PhD fellowship (Mexican Government), and is a fellow of the Franco-German Integrative Biology of

Infection and Diseases (IB-ID) doctoral program (Université Franco-Allemande, UFA). PAP also received funding from an EMBO Scientific Exchange Grant.

## Author contributions

JL conceived the project; MG, JJ, DR performed in vivo experiments; MG, EE, PA, and SF performed in vitro and molecular experiments; MG, EE, PA, and SF analyzed the data; JL supervised the work; MG and JL wrote the manuscript.

## Competing interests

JL patented DNM2 downregulation for centronuclear myopathy treatment. The remaining authors declare no competing interests.

## Additional information

**Supplementary information** The online version contains supplementary material available at <https://doi.org/10.1038/s41467-025-59925-6>.

**Correspondence** and requests for materials should be addressed to Jocelyn Laporte.

**Peer review information** *Nature Communications* thanks the anonymous reviewer(s) for their contribution to the peer review of this work. A peer review file is available.

**Reprints and permissions information** is available at <http://www.nature.com/reprints>

**Publisher's note** Springer Nature remains neutral with regard to jurisdictional claims in published maps and institutional affiliations.

**Open Access** This article is licensed under a Creative Commons Attribution-NonCommercial-NoDerivatives 4.0 International License, which permits any non-commercial use, sharing, distribution and reproduction in any medium or format, as long as you give appropriate credit to the original author(s) and the source, provide a link to the Creative Commons licence, and indicate if you modified the licensed material. You do not have permission under this licence to share adapted material derived from this article or parts of it. The images or other third party material in this article are included in the article's Creative Commons licence, unless indicated otherwise in a credit line to the material. If material is not included in the article's Creative Commons licence and your intended use is not permitted by statutory regulation or exceeds the permitted use, you will need to obtain permission directly from the copyright holder. To view a copy of this licence, visit <http://creativecommons.org/licenses/by-nc-nd/4.0/>.

© The Author(s) 2025